

A new method of reconstructing Galactic three-dimensional structures using ultralong-wavelength radio observationsYANPING CONG,^{1,2} BIN YUE,¹ YIDONG XU,¹ YUAN SHI,^{1,2} AND XUELEI CHEN^{1,2,3,4}¹*National Astronomical Observatories, Chinese Academy of Sciences, 20A Datun Road, Chaoyang District, Beijing 100101, China*²*School of Astronomy and Space Science, University of Chinese Academy of Sciences, Beijing 100049, China*³*Department of Physics, College of Sciences, Northeastern University, Shenyang, 110819, China*⁴*Center of High Energy Physics, Peking University, Beijing 100871, China***ABSTRACT**

The free-free absorption of low frequency radio waves by thermal electrons in the warm ionized medium of our Galaxy becomes very significant at $\lesssim 10$ MHz (ultralong-wavelength), and the absorption strength depends on the radio frequency. Upcoming space experiments such as the Discovering Sky at the Longest wavelength (DSL) and Farside Array for Radio Science Investigations of the Dark ages and Exoplanets (FARSIDE) will produce high-resolution multi-frequency sky maps at the ultralong-wavelength, providing a new window to observe the Universe. In this paper we propose that from these ultralong-wavelength multi-frequency maps, the three-dimensional distribution of the Galactic electrons can be reconstructed. This novel and robust reconstruction of the Galactic electron distribution will be a key science case of those space missions. Ultralong-wavelength observations will be a powerful tool for studying the astrophysics relevant to the Galactic electron distribution, for example, the impacts of supernova explosions on electron distribution, and the interaction between interstellar atoms and ionizing photons escaped from the HII regions around massive stars. An animation shows the reconstructed results using NE2001 model as input test. On ArXiv, it is given in the directory: Ancillary files. In the paper the animation is linked to Fig. 5.

Keywords: Interstellar medium (847) — Interstellar plasma (851)— Interstellar absorption (831)— Milky Way Galaxy (1054) — Radio interferometers (1345)

1. INTRODUCTION

Understanding our neighborhood and environment has long been a human pursuit, and the vicinity of the Solar system is of great interest, as it has direct impacts on the Solar system. Besides the well-observed nearby stars (Gaia Collaboration et al. 2022) the space is permeated with the interstellar medium (ISM), which serves as the reservoir of the material from which stars formed. Our Sun resides in a low-density cavity named “Local Bubble” (LB) or “Local Hot Bubble” (LHB, Cox & Reynolds 1987), which is filled with X-ray-emitting hot gas (Snowden et al. 1998). The LB has a typical electron number density of $\sim 5 \times 10^{-3} \text{ cm}^{-3}$, which is only $\sim 20\% - 50\%$ of the average value at that radius on the Galactic disk (Ocker et al. 2020), and it extends to ~ 100 pc (Frisch et al. 2011). This low density cavity in the ISM is thought to be created by a series of supernova explosions in prehistoric

time (Zucker et al. 2022). The spatial distribution and morphology of the ISM reflects the complex interactions between the gas and stars in the Galactic “ecosystem”, but our knowledge of this neighborhood is far from complete. For example, the Loop I bubble is another low density cavity adjacent to the LB, and the well-known giant North Polar Spur (NPS) feature in low-frequency radio sky maps is believed by many to be the brightest part of its bubble shell (Wolleben 2007). However, there are also arguments that the NPS is located at the much more distant Galactic Center and is related to the Fermi Bubble (Sarkar 2019).

The ISM has a number of different components or phases, which are observed or probed by various methods (Draine 2011). The atomic and molecular hydrogen, accounting for $\sim 80\%$ of the ISM hydrogen in mass, are traced by the 21cm and CO lines respectively. The dust ($\sim 1\%$ of ISM in mass) is measured using interstellar extinction (Lallement et al. 2014; Capitanio et al. 2017). The hot gaseous halo ($\lesssim 5\%$ of ISM mass within Galactocentric distance of ~ 20 kpc) is measured from the X-ray absorption or emission lines of highly ionized metals (Miller & Bregman 2013). The diffuse warm ionized

medium (WIM), which occupies $\sim 20 - 30\%$ of the volume near the Galactic plane and accounts for $\sim 30\%$ of the total ISM mass (Reynolds 1991a; Kulkarni & Heiles 1988), has been observed via the diffuse $H\alpha$ or other faint nebular emission lines (Reynolds 1977; Reynolds & Haffner 2000; Haffner et al. 2003; Finkbeiner 2003; Dickinson et al. 2003), or by the pulsar dispersion measures (DM) which could be used to reconstruct the 3D distribution of the electrons (Cordes et al. 1991; Taylor & Cordes 1993; Ferrière 2001; Gómez et al. 2001; Schnitzeler 2012; Greiner et al. 2016; Ocker et al. 2020), though the spatial resolution is limited by the available pulsars. Moreover, the scattering measure (SM) can provide information on the intrinsic fluctuations of the WIM (Williamson 1972).

The ISM can be probed using low-frequency radio observations, based on the fact that the ionized gas has a stronger absorption of radio waves at lower frequencies. The radiative transfer equation of the radiation is

$$\frac{dI_\nu}{ds} = -\alpha_\nu I_\nu + j_\nu \quad (1)$$

where I_ν is the intensity at frequency ν , and the absorption coefficient α_ν of the ISM at low radio frequency is dominated by the electron free-free process¹, given by (Condon & Ransom 2016)

$$\alpha_\nu \approx 3.28 \times 10^{-7} \left(\frac{T_e}{10^4 \text{K}} \right)^{-1.35} \left(\frac{\nu}{\text{GHz}} \right)^{-2.1} \left(\frac{n_e}{\text{cm}^{-3}} \right)^2 \text{pc}^{-1}, \quad (2)$$

where T_e and n_e are the free electron temperature and number density respectively. For diffuse Galactic electrons the absorption effect becomes significant at $\nu \lesssim 10$ MHz, while for dense HII regions the absorption becomes significant at even higher frequencies. The absorption strength contains information of electron densities at different distances. By using the multi-frequency data, the density distribution of the electron can be reconstructed, if the radiation emissivity j_ν (or in terms of brightness temperature $T = \frac{c^2 I_\nu}{2k\nu^2}$, $\epsilon = \frac{c^2 j_\nu}{2k\nu^2}$) is known. As this method is sensitive to free electron density, it probes primarily the WIM component of the ISM. Given the large volume and mass fraction of the WIM, it is obviously highly interesting and useful to reconstruct its 3D structures.

The data at frequencies below 30 MHz, which we shall refer to as the *ultralong-wavelength* band, and especially below 10 MHz, is very scarce, as ground-based observation is hindered by ionosphere and radio frequency interference (RFI) (Jester

& Falcke 2009). There were some ground-based observations at Tasmania of Australia and Canada (e.g. Reber & Ellis 1956; Ellis et al. 1962; Ellis & Hamilton 1966a; Cane & Whitham 1977; Cane 1979; Reber 1994, for its history see also Orchiston et al. 2015a; George et al. 2015a,b; Orchiston et al. 2015b; George et al. 2015c, 2016); and some early space observation (e.g. Hartz 1964; Alexander & Stone 1965; Smith 1965; Alexander et al. 1969; Brown 1973; Alexander & Novaco 1974; Novaco & Brown 1978; Manning & Dulk 2001). From these observations, it is noted that there is a downturn in the global brightness below ~ 3 MHz, which is believed to be caused by the free-free absorption mechanism of the ISM (Ellis et al. 1962; Alexander & Stone 1965; Ellis & Hamilton 1964; Novaco & Brown 1978). It has also been noted that at frequencies below a few MHz, in contrast to higher frequencies, the Galactic poles appear to be brighter than the Galactic plane, which is attributed to the stronger absorption on the Galactic plane (Alexander et al. 1970; Brown 1973; Novaco & Brown 1978; Ellis 1982; Manning & Dulk 2001).

Information on the Galactic electron distribution had been inferred from the ultralong-wavelength observations, even with the crude data obtained in the early observations. From the measured ultralong-wavelength global spectrum, by assuming an absorption length, electron density were derived (Hoyle & Ellis 1963; Smith 1965; Ellis & Hamilton 1966b; Alexander et al. 1970; Brown 1973; Cane 1979; Kassim 1989; Fleishman & Tokarev 1995), which is found to be $\sim 0.03 - 0.1 \text{ cm}^{-3}$ near the Galactic plane. These early works assumed a simple constant electron density. A slightly more sophisticated model assumes that the electron density depends on the vertical distance to the Galactic plane, which is constrained by pulsar DM (e.g. Reynolds 1991b; Nordgren et al. 1992; Taylor & Cordes 1993; Gómez et al. 2001). Peterson & Webber (2002) found however that in this model the electron density derived from the pulsar observations is too low to give rise the observed downturn of the ultralong-wavelength global spectrum. To fit both observations, they suggested that the electrons in the WIM is clumpy, which would induce stronger free-free absorption.

Jones et al. (2016) proposed that the free-free absorption can change the spectral index of the extragalactic background sources, and this can be used to construct the 2D distribution of electrons (the column density along the line of sight). However, by using discrete point sources as the background, this approach would be limited by the number of available point sources, just as in the pulsar observations.

The existing ultralong-wavelength observations have relatively low resolution. However, reconstruction of the full 3D Galactic electron structures will be feasible when high resolution ultralong-wavelength sky maps are available. Recently, a number of ultralong-wavelength space missions have

¹ The synchrotron self-absorption is unimportant for the typical Galactic magnetic field ($\sim 1 \mu\text{G}$) (Sun et al. 2008) and cosmic ray density ($\sim 10^{-13} \text{ GeV}^{-1} \text{ cm}^{-3}$) (Peron et al. 2021) above $\sim 1 \text{ kHz}$ (Ghisellini 2013). The radio wave cannot propagate below the ISM plasma frequency $\sim 2 \text{ kHz}$ (Jester & Falcke 2009), so in the frequency range considered in this paper, free-free absorption is the dominant absorption mechanism.

been proposed (Chen et al. 2019), such as the Discovering the Sky at the Longest wavelength (DSL) lunar orbit array (Chen et al. 2020; Shi et al. 2022b,a), and the Farside Array for Radio Science Investigations of the Dark ages and Exoplanets (FARSIDE) (Burns et al. 2019), which have the capability of producing high resolution maps, and will enable the full 3D reconstruction. Anticipating high resolution multi-frequency sky maps in the near future, we propose here to reconstruct the full 3D distribution of electrons using the ultralong-wavelength observation. The spatial distribution of the electrons is encoded in the spectrum: at the lower frequency, there is a higher contribution of absorption from more nearby absorption. If the emissivity along a line of sight (LoS) is known, then the electron density profile along it can be uniquely determined from a high resolution spectrum, without requiring any prior information about the density profile. Combining the observations of many LoS toward different directions one can obtain the full 3D distribution of the electrons. To our knowledge, such multi-frequency tomographic method has not been applied to the full reconstruction of the ISM before.

The sky radio radiation at different frequencies is produced by various physical processes. Besides the Cosmic Microwave Background (CMB), the thermal emission of the Galactic dust dominates the radiation above ~ 60 GHz. The sky between $\sim 10 - 60$ GHz is dominated by the bremsstrahlung radiation from Galactic thermal electrons. In this frequency range, there is also the spinning dust emission that peaks at ~ 20 GHz. Below ~ 10 GHz, the synchrotron radiation produced by the Galactic cosmic ray electrons increases rapidly and becomes dominant (de Oliveira-Costa et al. 2008). In the synchrotron background, roughly one-third (Seiffert et al. 2011) is from extragalactic sources such as star-forming galaxies, AGNs, galaxy clusters, and so on (Singal et al. 2018). Our proposed reconstruction depends on the observation of the ultralong-wavelength radiation, and the understanding of the unabsorbed synchrotron emissivity. The unabsorbed synchrotron radiation has a nearly power-law spectrum, and the variation of the spectral index is relatively small, which simplifies the reconstruction.

The outline of this paper is: In Sec. 2 we introduce our methods. In Sec. 3 we present the statistics of our results, and show the reconstructed 1D, 2D (Galactic plane) and 3D structures in simulations and compare them with the input electron model. In Sec. 4 we summarize the results and discuss some potential uncertainties.

2. METHODS

At the frequency of interest, the emissivity is dominated by the synchrotron radiation from cosmic ray electrons, which are believed to be produced primarily by supernova remnants and other accelerators and propagate over the Galaxy (Or-

lando & Strong 2013a). Due to the diffusive propagation, its intensity is relatively smooth, though it can be enhanced near the injecting source or at regions with stronger magnetic field which can trap the particles. Here, we model the emissivity as (Cong et al. 2021)

$$\epsilon(\nu, R, Z) = A \left(\frac{R + r_1}{R_0} \right)^\alpha e^{-R/R_0} e^{-|Z/Z_0|^\gamma} \left(\frac{\nu}{\nu_*} \right)^{\beta_G}. \quad (3)$$

where R, Z are the Galactic cylindrical coordinates, $r_1 = 0.1$ kpc is a small cut-off radius, $\nu_* = 408$ MHz, A, R_0, α, Z_0 and γ are model parameters, they are obtained by fitting the Haslam 408 MHz map (Haslam et al. 1982; Remazeilles et al. 2015). That is, we integrate this emissivity along each LoS to obtain a sky map at 408 MHz, then find the best-fit emissivity parameters for which the sky map is closest (measured by the Euclidean distance) to the observed map. Details can be found in Cong et al. (2021). We use the constant $\beta_G = -2.51$ that is fitted from multi-frequency observations between 45 - 408 MHz.

The purpose of this paper is to demonstrate the feasibility of the algorithm, therefore the simple emissivity model of Eq. (3) is used. One may also use more sophisticated models, for example the emissivity constructed by cosmic ray propagation and magnetic distribution model, and constrained by observations like gamma-ray sky maps, e.g. GALPROP (Porter et al. 2021). Moreover, there have been some attempts to construct the synchrotron emissivity from observations. The opaque HII regions can fully absorb the synchrotron radiation behind them. Therefore they can be used to separate the synchrotron emission from regions in front of and behind the HII regions (Nord et al. 2006; Hindson et al. 2016; Su et al. 2017, 2018; Polderman et al. 2019).

We make the mock multi-frequency sky maps $T_{\text{sky}}^{\text{obs}}(\nu_j, l, b)$ using the ULSA sky model (Cong et al. 2021). The ULSA generates the sky maps at ultralong-wavelengths including the free-free absorption effect of the Galactic electrons. There are a number of Galactic electron distribution models by synthesizing different observations (Cordes et al. 1991; Gaensler et al. 2008; Schnitzeler 2012; Yao et al. 2017), here the NE2001 model (Cordes & Lazio 2002, 2003) is adopted. The basic distribution is described by a few components with analytical formulae, for example the thin and thick Galactic disks, and the spiral arms. Known structures such as voids and dense HII regions are also added. Fluctuations caused by unresolved small-scale (< 1 pc) electron structures are described by fluctuation parameters. When simulating the mock sky maps, we adopt the same fluctuation parameter for all the electron components in NE2001 for simplicity. Cong et al. (2021) found that using the default fluctuation parameters in NE2001 would over-predict the sky brightness below ~ 3 MHz. Instead, if increasing the fluctuation parameter for the thick disk from $0.2 \text{ pc}^{-2/3}$ to $3.0 \text{ pc}^{-2/3}$, the predicted global

spectrum is consistent with the current observations. Since the thick disk dominates the all-sky absorption, we adopt the fluctuation parameter $3.0 \text{ pc}^{-2/3}$ for all components. The produced sky maps are similar to those in Fig. 8 of Cong et al. (2021). Meanwhile, as our reconstruction relies on the free-free absorption, adopting a larger fluctuation parameter, and hence a more efficient absorption effect, is helpful for reconstructing the electron content. Moreover, we adopt a constant electron temperature of 8000 K. In Fig. 1 we plot the mock sky maps $T_{\text{sky}}^{\text{obs}}(\nu_j, l, b)$ at $\nu = 0.1$ and 0.5 MHz respectively as examples. For sky maps at ≥ 1 MHz, we refer interested readers to the Fig. 8 of Cong et al. (2021).

We demonstrate the reconstruction of electron density distribution from the mock maps. The sky is pixelized with the HealPix scheme, with NSIDE=32, so there are a total of 12,288 pixels for the full sky. Better performance is expected if observations have higher resolutions. Along each pixel direction, the LoS is divided into N bins, each with an emissivity and electron density. The emissivity which is dominated by the synchrotron is assumed to be known. The sky brightness temperature of this LoS is modeled as

$$T_{\text{sky}}(\nu, l, b) \approx \sum_{i=1}^N \bar{\epsilon}_i(\nu, R, Z) \Delta x_i \frac{1 - \exp(-\Delta\tau_i)}{\Delta\tau_i} \exp(-\tau_{i-1}) + T_E^{\text{iso}}(\nu) \exp(-\tau_N), \quad (4)$$

where $\bar{\epsilon}_i$, Δx_i and $\Delta\tau_i$ are the mean emissivity, length and optical depth of the i -th bin, and

$$\tau_{i-1} = \sum_{i'=1}^{i-1} \Delta\tau_{i'}. \quad (5)$$

$T_E^{\text{iso}}(\nu)$ is the isotropic extragalactic background used in ULSA model, given by $T_E^{\text{iso}} = 1.2(\nu/\text{GHz})^{-2.58} \text{ K}$ (Seiffert et al. 2011).

We make log-spaced bins along the LoS, starting from $x_{\text{min}} = 0.005 \text{ kpc}$ with a step-interval of $\Delta \log x = 0.2$, as the brightness temperature is related to the exponential of optical depth. We have limited the LoS to a distance at most 20 kpc from the Galactic center. The free-free optical depth of each bin is

$$\begin{aligned} \Delta\tau_i &= \alpha_{\nu,i} \Delta x_i \\ &= 3.28 \times 10^{-7} \left(\frac{T_e}{10^4 \text{ K}} \right)^{-1.35} \left(\frac{\nu}{\text{GHz}} \right)^{-2.1} \left(\frac{\langle n_{e,i}^2 \rangle}{\text{cm}^{-6}} \right) \frac{\Delta x_i}{\text{pc}}. \end{aligned} \quad (6)$$

If T_e is known, then the reconstructed quantity is $\langle n_{e,i}^2 \rangle$. Here the symbol “ $\langle \rangle$ ” denotes the mean inside each bin. From

$\langle n_{e,i}^2 \rangle = F_{\text{fluc}} \langle n_{e,i} \rangle^2$, and if the fluctuation parameter² F_{fluc} is further known, it is translated into $\langle n_{e,i} \rangle$. For demonstration purpose we assume $T_e = 8000 \text{ K}$ (Reynolds 1990) and $F_{\text{fluc}} \equiv 3.0$ is known, to show the reconstructed electron density as result. Otherwise, our method only reconstructs a combined quantity $T_e^{-1.35} F_{\text{fluc}} \langle n_{e,i} \rangle^2$. In observations T_e varies between 5500 K and 20000 K (Reynolds 1990) or 6000 K - 10000 K (Haffner et al. 2009 and references therein), and F_{fluc} can be ≥ 3 (Gaensler et al. 2008). We assume that the emissivity $\epsilon(\nu, R, Z)$ is known and take the form as given by Eq. (3).

For the multi-frequency maps, we assume the frequency interval is 0.1 MHz for the frequency range of 0.1-1.0 MHz, and 0.2 MHz for the frequency range of 1.0 to 10.0 MHz, so there are totally 55 mock maps at 55 frequencies. We treat $\langle n_{e,i} \rangle$ of each bin as an unknown parameter. By comparing the multi-frequency sky brightness temperature Eq. (4) that is a function of $\langle n_{e,i} \rangle$, with observations (mock maps), we can simultaneously find $\langle n_{e,i} \rangle$ of all bins that minimize

$$\chi^2(l, b) = \sum_{j=1}^{N_{\text{freq}}} \frac{[T_{\text{sky}}(\nu_j, l, b) - T_{\text{sky}}^{\text{obs}}(\nu_j, l, b)]^2}{\sigma_{\text{noise}}^2}, \quad (7)$$

using the MCMC procedure (Foreman-Mackey et al. 2013), where N_{freq} is the number of frequency bins.

In this work we use fixed grids for solving the electron densities, which may not accurately capture some small and dense clumps. The absorption by a single dense clump may obscure the whole LoS, but if we already know some information about these clumps, i.e. their location, size, and density from other observations, we can use such information to improve the fitting. If a bin contains a dense clump, then the density contribution from this clump to the bin is known, leaving only the diffuse electron density as an unknown quantity. For those dense clumps with extremely strong absorption, data at higher frequencies can also be employed. We assume that clumps with density $> 0.1 \text{ cm}^{-3}$ have been known. For these LoS we add 20 frequency points between 10 and 30

² When converting the $\langle n_e^2 \rangle$ into $\langle n_e \rangle$, we define fluctuation parameter $F_{\text{fluc}} = \langle n_e^2 \rangle / \langle n_e \rangle^2$. It is a dimensionless and phenomenological parameter that describes the connection between the electron density and the free-free absorption strength, without specifying a physical picture of the electron distribution. In NE2001, the physically motivated fluctuation parameter is defined as $F_{\text{NE2001}} = \zeta \omega^2 \eta^{-1} l_0^{-2/3}$, where ω^2 (to avoid confusing the variable emissivity, in this paper we replace the “ ϵ^2 ” in NE2001 paper with “ ω^2 ”) describes the electron fluctuations inside electron clouds, ζ describes the cloud-to-cloud fluctuations, η is the filling factor of electron clouds, and l_0 is their outer scale. Therefore F_{fluc} performs as $l_0^{2/3} F_{\text{NE2001}} \omega^{-2} (1 + \omega^2)$ in formula. We have checked that when $l_0 = 1 \text{ pc}$ is adopted as in NE2001, the same F_{fluc} and F_{NE2001} values give the same conversion factors. For this reason, we keep the dimensionless definition of the fluctuation parameter as it is only used to display the reconstruction results more intuitively.

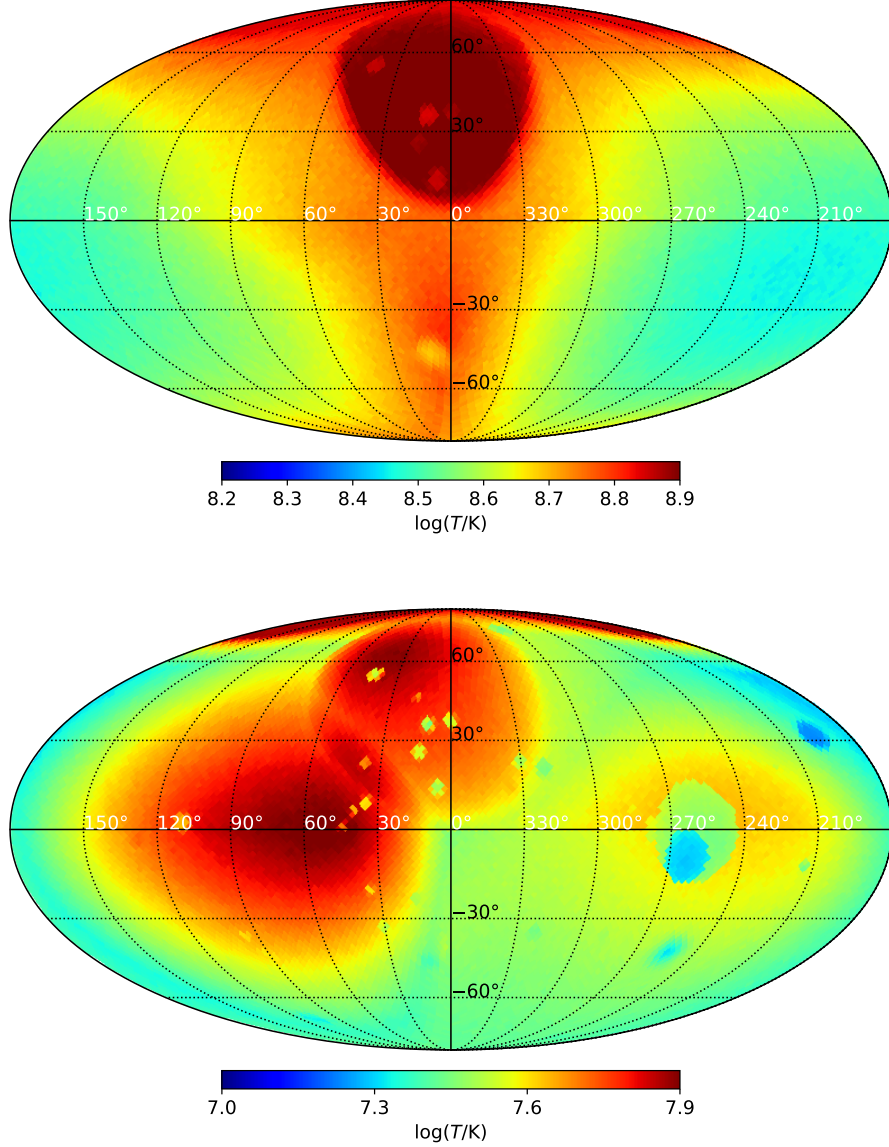


Figure 1. The mock sky maps at 0.1 MHz (top) and 0.5 MHz (bottom) used in this paper.

MHz, with an interval of 1 MHz. The solution may also be improved with adaptive grids, but we leave such technical improvements to future works.

Regarding the noise level of the observations, at low-frequency the system temperature is dominated by the sky temperature (Shi et al. 2022b),

$$\begin{aligned} \sigma_{T_{\text{noise}}} &\sim \frac{D^2 T_{\text{sky}}}{A_{\text{eff}} \sqrt{N_a(N_a - 1) t_{\text{obs}} \Delta \nu}} \\ &= \frac{4\pi T_{\text{sky}}}{\theta_{\text{res}}^2 \sqrt{N_a(N_a - 1) t_{\text{obs}} \Delta \nu}}, \end{aligned} \quad (8)$$

where $A_{\text{eff}} = \frac{\lambda^2}{4\pi}$ is the effective area of the antenna with physical size $\ll \lambda$; N_a is the number of antennas; D is the

baseline length, and $\theta_{\text{res}} \sim \frac{\lambda}{D}$ is the angular resolution; t_{obs} is the integration time and $\Delta \nu$ is the width of the frequency point. For $\theta_{\text{res}} = 1^\circ$, $N_a = 8$ and $\Delta \nu = 0.1$ MHz, we have $\sigma_{T_{\text{noise}}}/T_{\text{sky}} \sim 1\%$ if $t_{\text{obs}} = 0.1$ year; and $\sigma_{T_{\text{noise}}}/T_{\text{sky}} \sim 10\%$ if $t_{\text{obs}} = 0.5$ day. We adopt 1% noise level for all simulations in this paper.

3. RESULTS

In Fig. 2 we show the minimum χ^2 normalized by the number of frequency bins for each LoS as HealPix sky map (top), and the probability density (PD) of their distribution (bottom). About 90% of the LoS have $\chi_{\text{min}}^2/N_{\text{freq}} < 1.5$, so the MCMC fitting does indeed have a good performance. About 2% of the LoS have $\chi_{\text{min}}^2/N_{\text{freq}} > 3.0$, for displaying

purpose they are not shown in Fig. 2. The distribution of $\chi_{\min}^2/N_{\text{freq}}$ is well-fitted by a Gaussian function with the peak 1.72, the center 1.12, and the radius 0.23. We check that most LoS with $\chi_{\min}^2/N_{\text{freq}} > 2.0$ have dense clumps. As described in Sec. 2, if there is a dense clump in a LoS, we assume that its contribution to the density in the relevant bin is known, and only fit the density of diffuse electrons in that bin. This can improve the reconstructed density profile, see Fig. 4 later on. But it cannot solve the problem completely. Because usually the size of the dense clump is much smaller than the bin width, its absorption to the emissivity in the bin also depends on its exact location inside the bin, but this information is not used in the fix grid computation. In the northern hemisphere between $-30^\circ \lesssim l \lesssim 30^\circ$ there is the Loop I bubble, it is a low density cavity with huge angular size, the absorption within the bubble is weak, see the sky maps in Fig. 1. Moreover, such a bubble has an edge that is modeled as a sharp break in the NE2001. The sharp break feature is hard to capture because of the bin resolution limit. Because of the above reasons, the $\chi_{\min}^2/N_{\text{freq}}$ in this region is biased to higher values.

We then compare our reconstructed electron density with NE2001³. The same fluctuation parameter of 3.0 is assumed for all gas components in order to translate the reconstructed $\langle n_e^2 \rangle$ into the mean electron density that is more intuitive for displaying. We plot the mean absolute value of relative errors between the reconstructed electron density and that of NE2001 $|\overline{f_{\text{err}}}|$ for all LoS as a map in the top panel of Fig. 3. To reduce the discrete errors, both the reconstructed density and the NE2001 density are smoothed by a Gaussian kernel with a radius equal to one bin width. For each LoS we only count the bins with $R < 12$ kpc and $|Z| < 2$ kpc, beyond that the electron density is too small and the absorption too weak for relative error to be a good indicator of the reconstruction performance. In the bottom panel of Fig. 3, we show the probability density distribution of $|\overline{f_{\text{err}}}|$. About 70% LoS have $|\overline{f_{\text{err}}}| < 20\%$. Most of them are near the Galactic plane, see top panel of Fig. 3. This is natural because in the Galactic plane the absorption is stronger, making it possible to reconstruct the electron density profile more accurately. High Galactic latitude regions have larger errors, not only because

the absorption is weaker, but also because the extragalactic background has a larger fraction in the total received flux. Around $l \sim 330^\circ$, there is a patch where the relative error is much higher than the surrounding regions. We check that in NE2001 there is a low density void with density as low as 0.001 cm^{-3} . In our reconstruction usually the low density regions have larger relative errors. Nevertheless, our reconstruction has good performance, considering the fact that in our method not only each LoS, but also the electron density in each bin of a LoS, are all independent of the others.

We show the reconstructed 1D density profiles for some LoS in Fig. 4 as examples. In Galactic plane our algorithm correctly reproduces the electron density profiles up to ~ 10 kpc, in high Galactic latitude regions up to ~ 3 kpc, although there are deviations on small scales. For all these LoS, within $\sim 0.03 - 0.2$ kpc, the electron density is relatively low, indicating that our Sun is located in a bubble. For the LoS pointing to $l \sim 90^\circ$ however, the low density environment extends to ~ 2 kpc, this is the low density region simply called “LDR” in the NE2001 model (Toscano et al. 1999; Cordes & Lazio 2003). A LoS penetrating the Gum Nebula is shown in (g) and (h) panels. Panel (g) is the result directly reconstructed, and panel (h) is the result when the location, size and density of Gum Nebula is known and its density is added to the relevant bin. Indeed, the density profile in panel (h) is much improved than in panel (g). Nevertheless, except for the Gum Nebula, other dense clumps have much smaller angular sizes on the sky, the large-scale morphology of our reconstructed maps almost does not change, if we simply remove those LoS penetrating dense clumps.

With the mock full-sky map, we can reconstruct the 3D distribution of Galactic electrons by synthesizing all LoS. The tomographic reconstruction result of our Sun’s vicinity is shown in the top panel of Fig. 5, and for comparison the original NE2001 model distribution is shown in the bottom panel. This figure uses 12288 LoS, and the density volume is a heliocentric cuboid of $6 \times 6 \times 4 \text{ kpc}^3$, with pixel size 0.05 kpc. However, the poorest resolution at the edge is ~ 0.5 kpc, limited by the bin width. The reconstructed volume map is also shown in a video linked to Fig. 5. Both the reconstructed density and the NE2001 density are smoothed by a Gaussian kernel with radius 0.05 kpc. Our method reconstructs major features from NE2001, including the LB, the LSB, the Gum Nebula, and so on.

In our reconstructed electron density field, there are some streaks as shown in the top panel of Fig. 5. This is a consequence of our solving the density along the radial direction from our position as the center. Since we adopt a grid along the radial direction, the grid cells will have shapes that either appear elongated if their size along the radial direction is larger than the tangential direction, or oblate if the reverse is true. In our case we adopted a log-spaced grid which is

³ By definition, the fluctuation parameter in NE2001 only accounts for the fluctuations on scales smaller than 1 pc. However, our bin width is much larger than 1 pc. So the fluctuations on scales larger than 1 pc and smaller than bin width are absorbed in the reconstructed quantity $\langle n_{e,i} \rangle$ for the i -th bin. For this bin, if we divide it into N_{sub} sub-bins with width of 1 pc, then in principle the reconstructed $\langle n_{e,i} \rangle$ should be more close to $\sqrt{\sum_j n_{e,j}^2/N_{\text{sub}}}$ rather than $\sum_j n_{e,j}/N_{\text{sub}}$, where $n_{e,j}$ is the NE2001 electron density of the j -th sub-bin in the i -th bin. However, in most cases these two quantities are close to each other, unless the bin width $\gtrsim 1$ kpc, or the bin contains dense clumps. Throughout this paper, when comparing with NE2001 model we take the quantity $\sqrt{\sum_j n_{e,j}^2/N_{\text{sub}}}$ of NE2001.

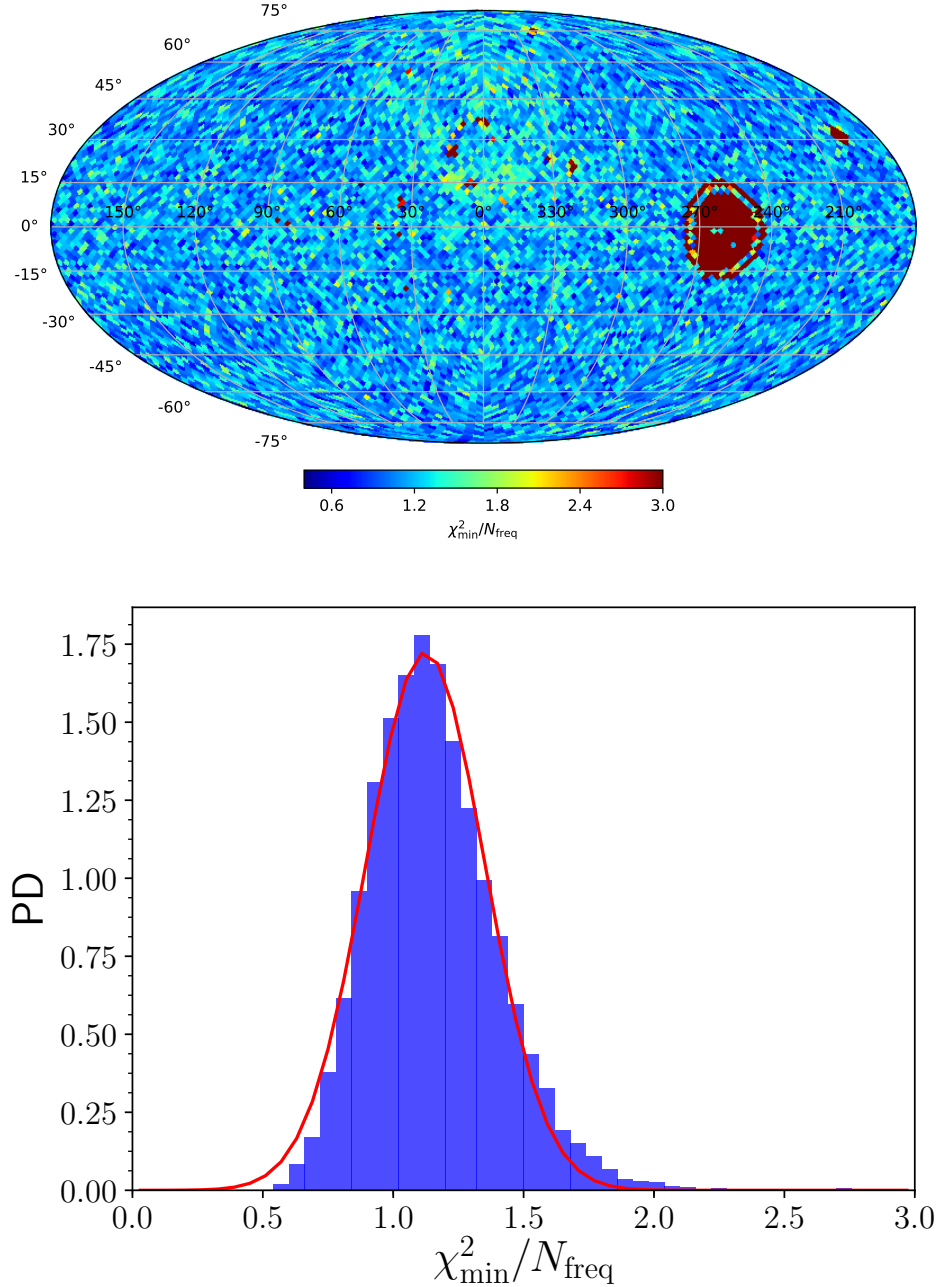


Figure 2. *Top:* The sky map of $\chi^2_{\min}/N_{\text{freq}}$ for all LoS. *Bottom:* The probability density of the $\chi^2_{\min}/N_{\text{freq}}$ distribution. The solid curve is a Gaussian fit, with the peak 1.72, the center 1.12 and the radius 0.23. There are about 2% of LoS have $\chi^2_{\min}/N_{\text{freq}} > 3.0$. For displaying purpose, in the top panel they are shown by color same to 3.0, while in the bottom panel these are not counted.

good for the numerical problem, but at the far end the streak is more apparent. Increasing the number of LoS and reducing the bin width can relieve the steak problem. However, if the bin width is too small then the noise of each bin is large since the contribution of a single bin to the total absorption is small.

In Fig. 6 we show the probability density as a function of $|f_{\text{err}}|$ and n_e , where $|f_{\text{err}}|$ is the absolute value of the relative error between the top and bottom panels of Fig. 5 for each

pixel, and n_e is the density of relevant pixel in the bottom panel of Fig. 5. About 70% pixels have $|f_{\text{err}}| < 30\%$, and the median of $|f_{\text{err}}|$ is 17%. About 8% pixels have $|f_{\text{err}}| > 100\%$, most of them are low-density regions, see the top left part of Fig. 6. This is not surprising because the absorption in low-density regions is weaker, therefore hard to constrain the density accurately. Considering the above, any structures with size comparable to the resolution limit and/or with density

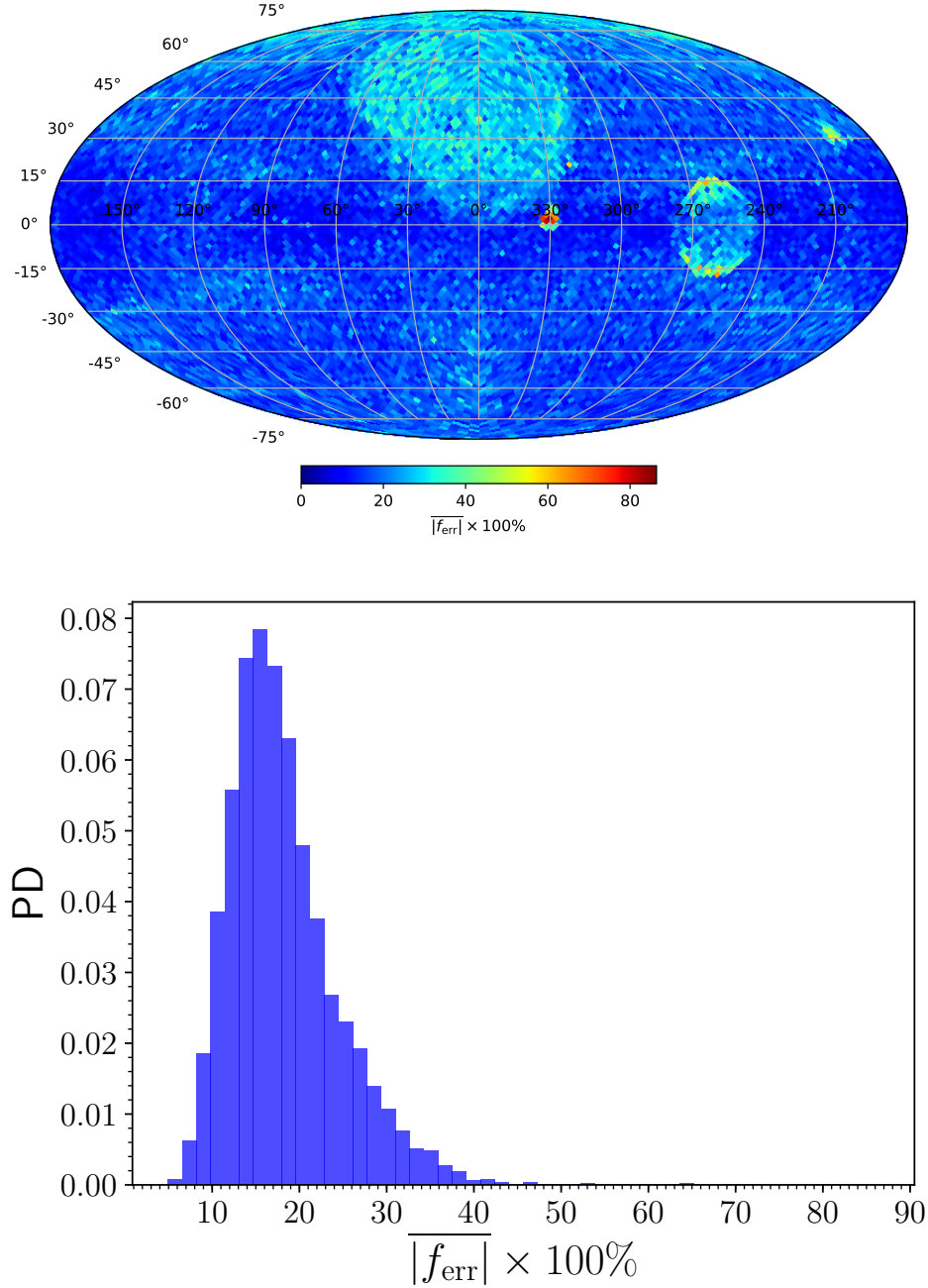


Figure 3. *Top:* The sky map for the mean absolute value of the relative error of all LoS. *Bottom:* The probability density of the mean absolute value of the relative error distribution.

contrast comparable to the uncertainty level are hard to see from the figure.

Moving further from our vicinity on to larger scales, we meet two spiral arms that bracket our Sun, as shown in the reconstructed electron density on the Galactic plane in Fig. 7. The reconstructed electron map clearly shows the Carina-Sagittarius arm in the direction towards the Galactic center, and the Perseus arm in the anti-center direction. Previously the spiral arms have been mapped via neutral hydrogen, CO

(trace the molecular hydrogen, Englmaier et al. 2011; Nakanishi & Sofue 2016), dust extinction survey (Rezaei Kh. et al. 2018), and other tracers for high-mass star formation (Hou & Han 2014). The Ultralong-wavelength observations will allow reconstruction of the diffuse free electrons in the spiral arms.

4. SUMMARY AND DISCUSSIONS

The ultralong-wavelength radio spectrum below ~ 10 MHz has largely been constrained from the ground and space

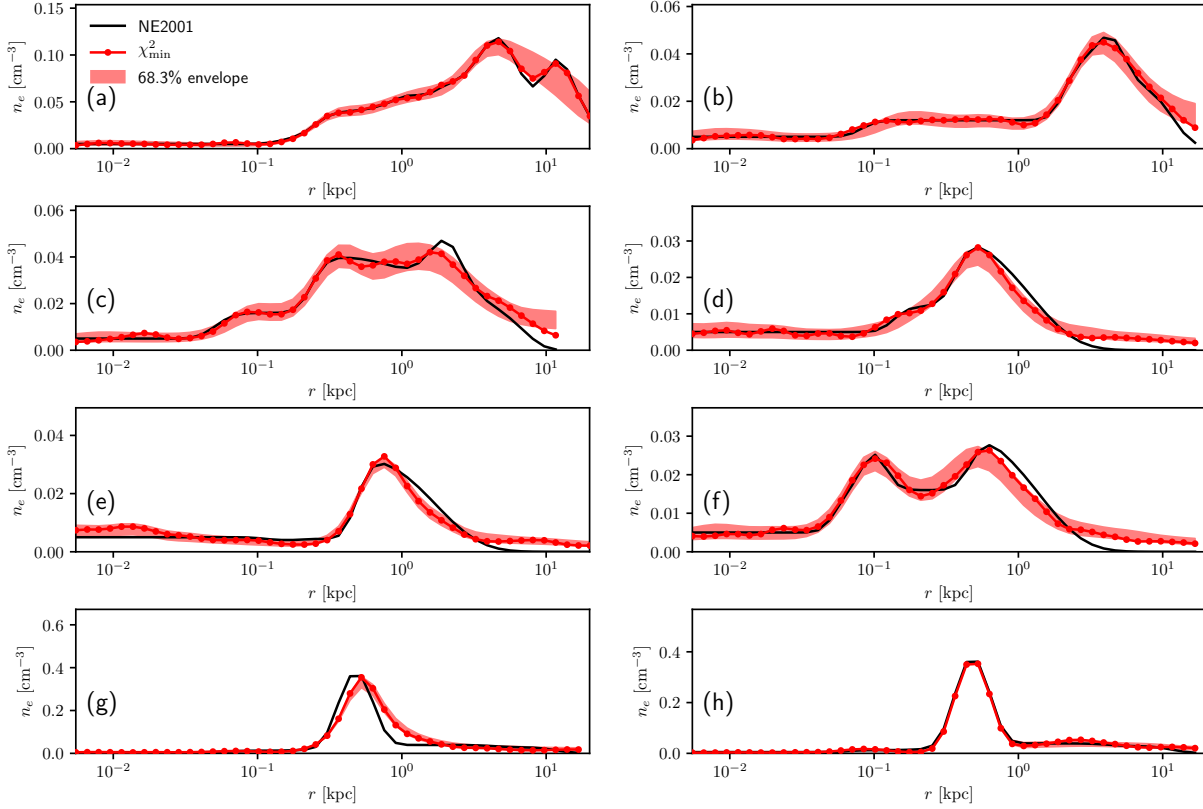


Figure 4. The reconstructed electron density profiles along 7 LoS in the Galactic plane and in high Galactic regions, pointing to different directions: (a) $l = 2^\circ$, $b = 0^\circ$; (b) $l = 90^\circ$, $b = 0^\circ$; (c) $l = 180^\circ$, $b = 0^\circ$; (d) $l = 101.67^\circ$, $b = 49.70^\circ$; (e) $l = 5.62^\circ$, $b = 34.23^\circ$; (f) $l = 260.16^\circ$, $b = -41.81^\circ$; (g) $l = 270^\circ$, $b = 0^\circ$, the bump at ~ 0.5 kpc is the Gum Nebula; (h) same as (g) but assume information on Gum Nebula on this LoS is already known, and $0.1 \leq \nu \leq 30$ MHz data is used for fitting. As comparison in each panel we also plot the NE2001 density of same r bins. In all panels the reconstructed results and the NE2001 model are smoothed by Gaussian kernel with radius equal to one bin.

at poor spatial resolution. Some space missions have been proposed to obtain high-resolution sky maps in this band. In this paper we proposed that, thanks to the frequency-dependent absorption to electromagnetic wave, from the upcoming ultralong-wavelength observations the three-dimensional structures of the Galactic electrons can be reconstructed. Using mock sky maps we performed simulations to prove the feasibility of this method.

There are dense clumps in the sky, and they often have active star formation and also emit synchrotron radiation. If such emission is not accurately known, then it may cause errors in reconstruction. To assess this uncertainty, we consider the nearby Gum Nebula. According to [Woermann \(1998\)](#), at 408 MHz the Gum Nebula has typical surface brightness temperature of roughly 10 K, and the typical spectrum index derived from 408 and 2326 MHz is roughly -2.5 . Taking the Gum Nebula as a sphere with radius 0.14 kpc and electron density 0.43 cm^{-3} , at a distance 0.5 kpc from us ([Cordes & Lazio 2002](#)), and the emissivity is uniformly distributed in the sphere, we expect $\sim 5 \times 10^4$ K surface brightness at 1 MHz if $F_{\text{fluc}} = 3.0$. This is actually smaller than the mean brightness of the Galactic plane in our sky model at the same

frequency. According to this simple estimate, a large fraction of the clump emission might be absorbed by itself, since it has density much higher than the ambient medium. So at least in this case, the influence of the clump emission is modest.

Our synchrotron emissivity model is cylindrical. However the real emissivity could have non-cylindrical large-scale structures, induced by the spiral structures in the regular magnetic field ([Orlando & Strong 2013b](#)). We have tested that for such a spiral emissivity model, the electron density can be still reconstructed and all conclusions do not change. The reconstruction errors could come from the unknown random small-scale fluctuations in the synchrotron emissivity. To estimate its impact, we add fluctuations to the emissivity model of Eq. (3), and then reconstruct the electron density profile assuming the small-scale fluctuations are not present. Motivated by the measured angular power spectrum of Galactic synchrotron radiation $C_l \propto l^{-2}$ ([Iacobelli et al. 2013](#)), we model the small-scale fluctuations of emissivity to be Gaussian with the power spectrum

$$P_\epsilon(k) \propto k^{-3}, \quad k > k_{\text{min}}, \quad (9)$$

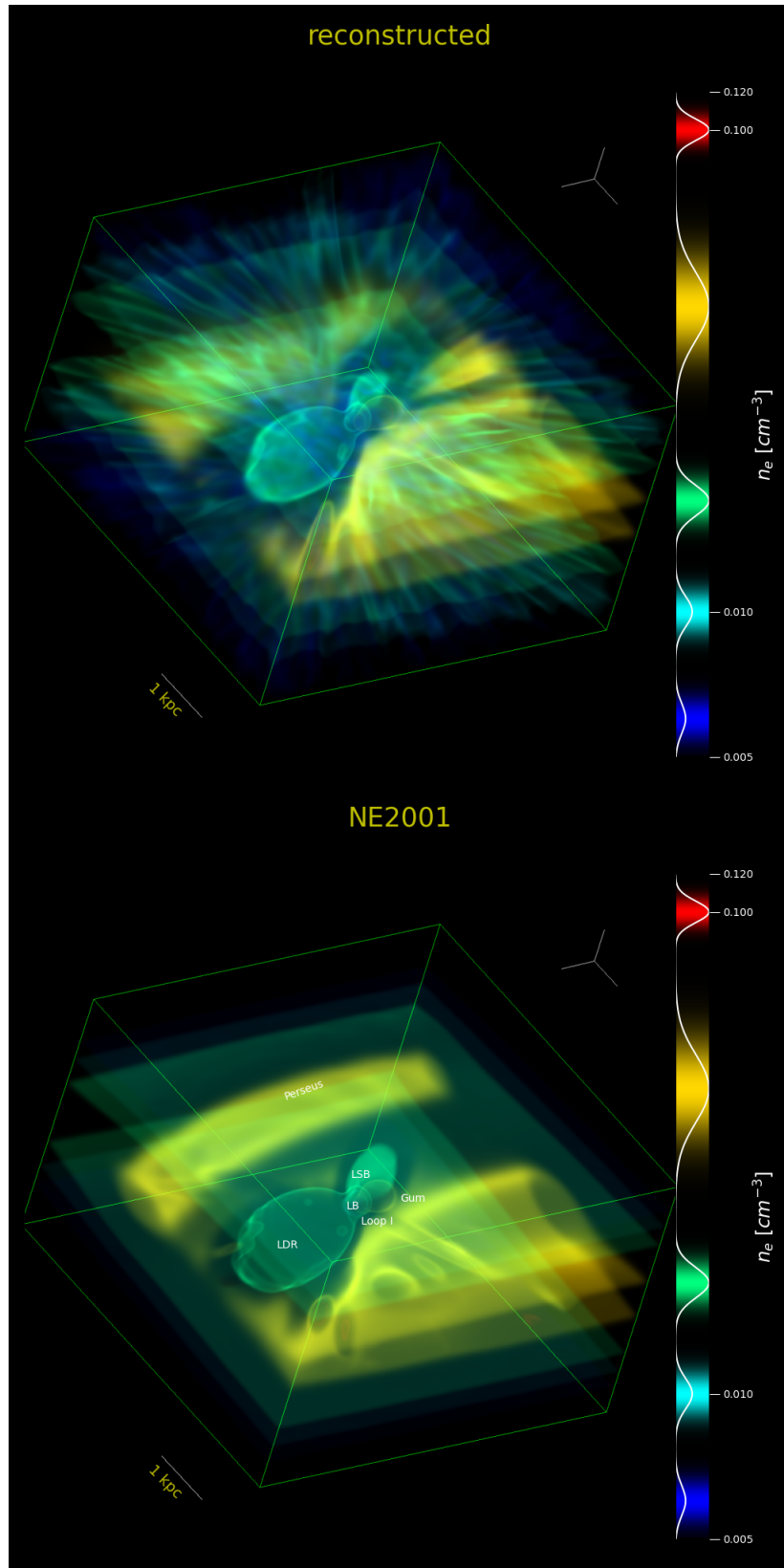


Figure 5. *Top:* The reconstructed electron distribution. *Bottom :* The NE2001 model. Both the top and bottom panel are smoothed by a Gaussian kernel with a radius of 0.05 kpc. An associated animation for the reconstructed electron density is available online. In the animation, the 3D box rotates about the Z-axis in the first 30 seconds duration, so one can see the structures from different perspectives. In the last 3 seconds, we zoom in the 3D box until the innermost LB is seen. (On ArXiv, please find the animation in the directory: Ancillary files)

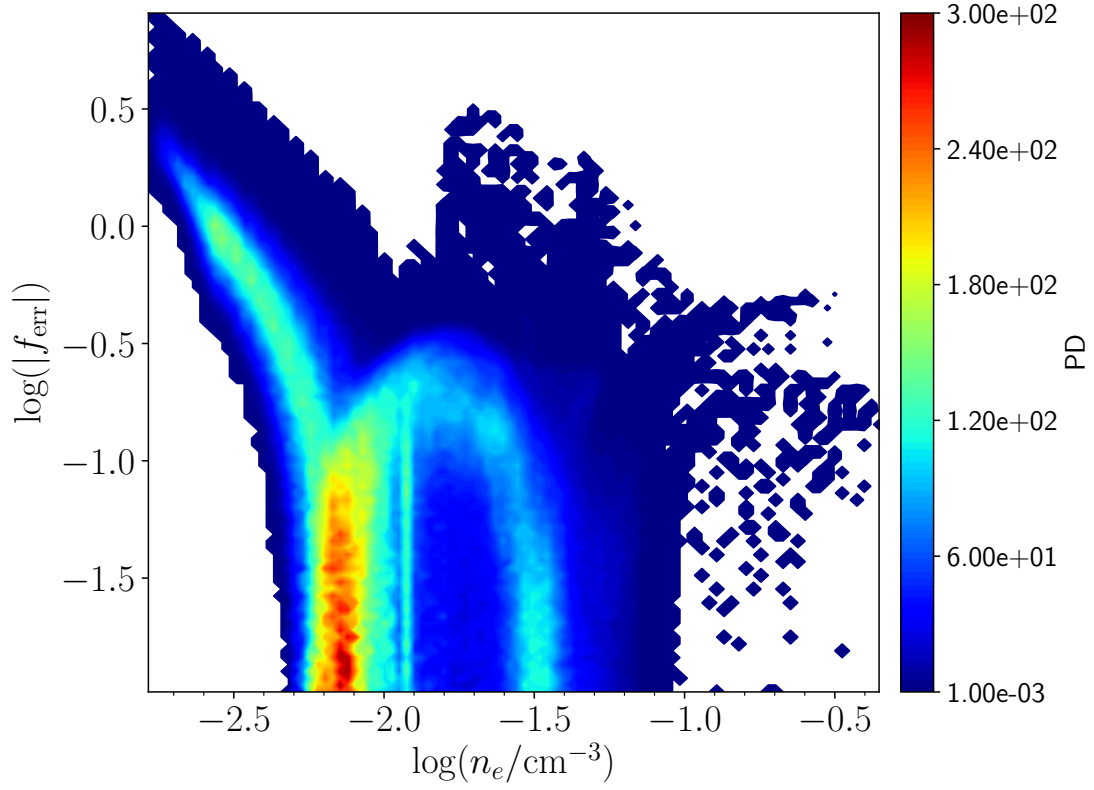


Figure 6. The $|f_{\text{err}}|$ vs. n_e in the reconstructed 3D Cartesian coordinate density field. Colorbar indicates the probability density with normalization $\int \text{PD} d|f_{\text{err}}| dn_e = 1$.

where k is the spatial wavenumber. We assume that fluctuations only exist on scales smaller than $2\pi/k_{\min}$ ($k > k_{\min}$). On larger scales, we assume the Eq. (3) correctly describes the cosmic ray emissivity. We normalize P_ϵ so that the emissivity has a mean relative fluctuations level $\sim 50\%$ at the smoothing scale 0.1 kpc. That is, when the fluctuations field following the power spectrum of Eq. (9) is added to the cylindrical emissivity field, and the new emissivity field is smoothed with Gaussian kernel with radius = 0.1 kpc, then $\sqrt{(\delta\epsilon)^2}/\bar{\epsilon} \sim 50\%$. We found that, despite this perturbation, which induces errors in the reconstruction at small scales, the reconstruction result remain largely unchanged at large scales. The results of this reconstruction are shown in Fig. 8, for $k_{\min} = 5.0 \text{ kpc}^{-1}$ and $k_{\min} = 0.5 \text{ kpc}^{-1}$ respectively.

Our method directly reconstructs $\langle n_e^2 \rangle$ of each bin, a quantity that produces absorption equivalent to real electron distribution inside this bin. Since $\langle n_e^2 \rangle = F_{\text{fluc}} \langle n_e \rangle^2$, we actually cannot distinguish the cases if a region has smaller electron density but larger fluctuation parameter, or the reverse, unless the F_{fluc} is derived from other methods. Just for convenience of translating the results into a more intuitive quantity $\langle n_e \rangle$ we assume a constant F_{fluc} . The F_{fluc} may vary bin-by-bin since the fluctuations of the WIM can depend on locations (Reynolds 1991a; Gaensler et al. 2008), however we have checked that it will not change our reconstruction of $\langle n_e^2 \rangle$. Just, if the correct F_{fluc} is not known, the translated $\langle n_e \rangle$ would deviate from the real mean electron density. For example, in Gaensler et al. (2008) they investigated the volume filling factor of electron clouds. If the electron fluctuations inside clouds are negligible, then the fluctuation parameter can be well approximated as the reciprocal of the filling factor. In this case the fluctuation parameter is ~ 25 in the Galactic plane and ~ 3 at $|Z| = 1.4 \text{ kpc}$. For such a fluctuation parameter then our $\langle n_e \rangle$ at Galactic plane is overestimated by a factor ~ 3 . In Ocker et al. (2021) they considered a complicated electron cloud model rather than uniform density. According to the observations of scattering and dispersion measures of the Galactic pulsars, they found that the fluctuation parameters at the low Galactic latitudes and inner Galaxy are $\gtrsim 10 - 1000$ times larger than the typical thick disk at high

latitudes. Considering this, the error on the reconstructed electron density by assuming a constant fluctuation parameter can be even much larger, particularly at low Galactic latitudes and for the LoS towards the inner Galaxy. Future studies trying to disentangle the electron density would merit a more sophisticated model for the spatial variation in the fluctuation parameter. Perhaps values independently inferred from pulsar observations along similar LoS could be employed, although this would be limited by the sparseness of pulsar spatial distribution. In some biased regions, the WIM has larger fluctuations. The synchrotron emissivity from such regions will be also biased, because usually such regions are more close to the sources of the cosmic ray–supernova remnants. We tested that, if the biased emissivity is correctly involved in the emissivity model, then no matter if the fluctuation parameter is biased or not in the same regions, the $\langle n_e^2 \rangle$ can still be correctly reconstructed. However if the biased emissivity is missed in the model, then like what we have discussed in last paragraph, it would induce small-scale uncertainties on the reconstructed $\langle n_e^2 \rangle$ and the final $\langle n_e \rangle$.

Despite some modeling uncertainties, the reconstruction from ultralong-wavelength observation is fairly robust. Once the ultralong-wavelength sky is systematically surveyed, we will gain new knowledge about our residence in the Milky Way, and pin down the long-lasting debate on the distance of the NPS. It will be an important step in obtaining a synthetic picture of our Galaxy.

ACKNOWLEDGMENTS

We thank the anonymous referee for the very helpful comments. This work is supported by National SKA Program of China Nos. 2020SKA0110402 and 2020SKA0110401, Inter-government cooperation Flagship program grant No. 2018YFE0120800, the National Natural Science Foundation of China grant Nos. 11973047, 11633004, the Chinese Academy of Sciences (CAS) Key Instrument grant ZD-KYYQ20200008, the Strategic Priority Research Program XDA15020200, and the CAS Frontier Science Key Project QYZDJ-SSW-SLH017.

REFERENCES

- Alexander, J. K., Brown, L. W., Clark, T. A., & Stone, R. G. 1970, *A&A*, 6, 476
- Alexander, J. K., Brown, L. W., Clark, T. A., Stone, R. G., & Weber, R. R. 1969, *ApJL*, 157, L163, doi: [10.1086/180411](https://doi.org/10.1086/180411)
- Alexander, J. K., & Novaco, J. C. 1974, *AJ*, 79, 777, doi: [10.1086/111608](https://doi.org/10.1086/111608)
- Alexander, J. K., & Stone, R. G. 1965, *ApJ*, 142, 1327, doi: [10.1086/148418](https://doi.org/10.1086/148418)
- Brown, L. W. 1973, *ApJ*, 180, 359, doi: [10.1086/151968](https://doi.org/10.1086/151968)
- Burns, J. O., Hallinan, G., Lux, J., et al. 2019, arXiv e-prints, arXiv:1911.08649. <https://arxiv.org/abs/1911.08649>
- Cane, H. V. 1979, *MNRAS*, 189, 465, doi: [10.1093/mnras/189.3.465](https://doi.org/10.1093/mnras/189.3.465)
- Cane, H. V., & Whitham, P. S. 1977, *MNRAS*, 179, 21, doi: [10.1093/mnras/179.1.21](https://doi.org/10.1093/mnras/179.1.21)

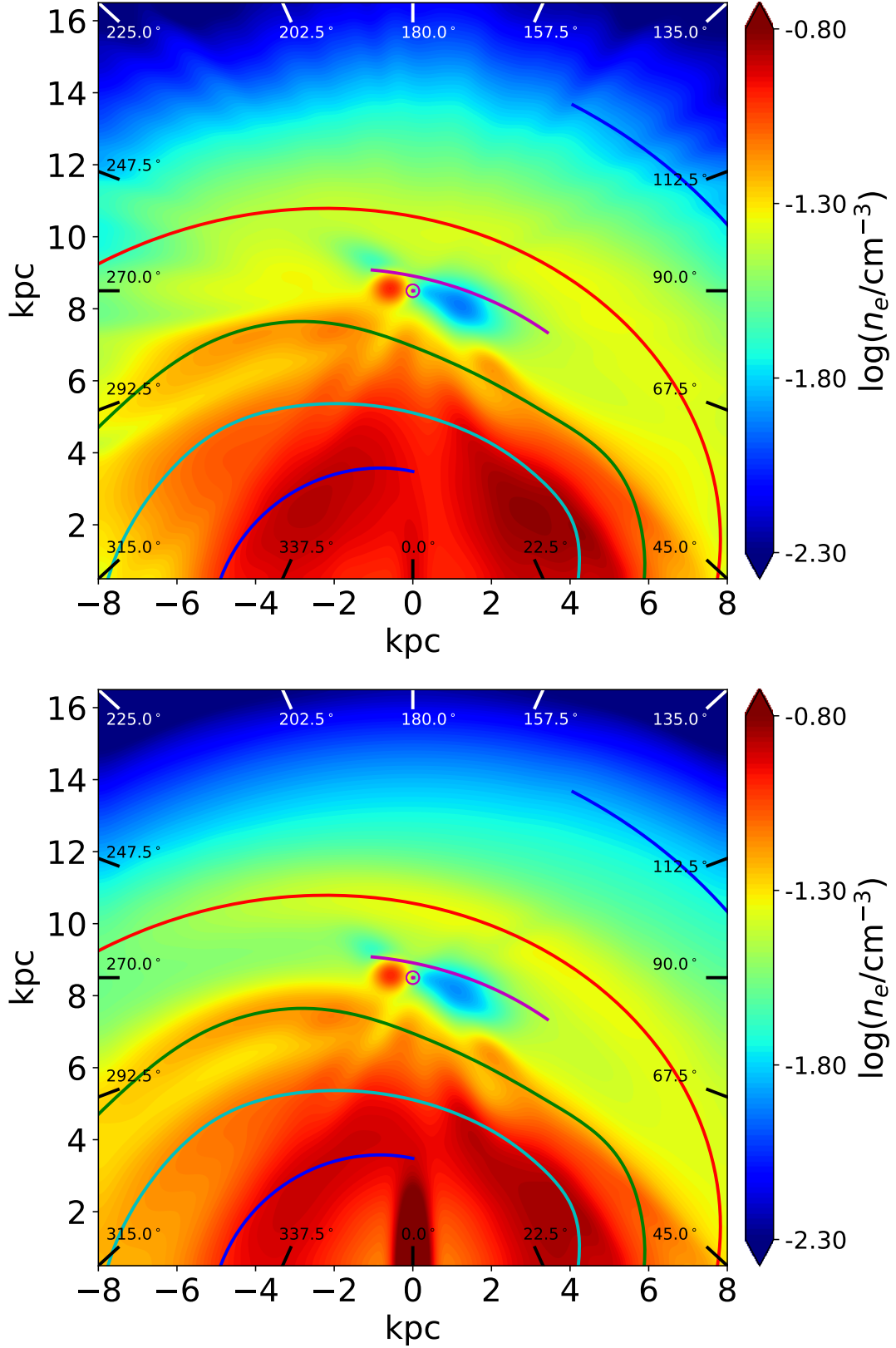


Figure 7. *Top:* The face on view of the electron distribution on Galactic plane reconstructed from 900 equally separated LoS. To suppress the noise and highlight the large-scale structures, the density fields are smoothed by Gaussian kernel with a radius 0.25 kpc. *Bottom:* The electron density in the NE2001 model. For comparison purpose, the NE2001 data is binned and smoothed same to reconstructed density. To guide the eye we plot the locations of spiral arms modeled in NE2001.

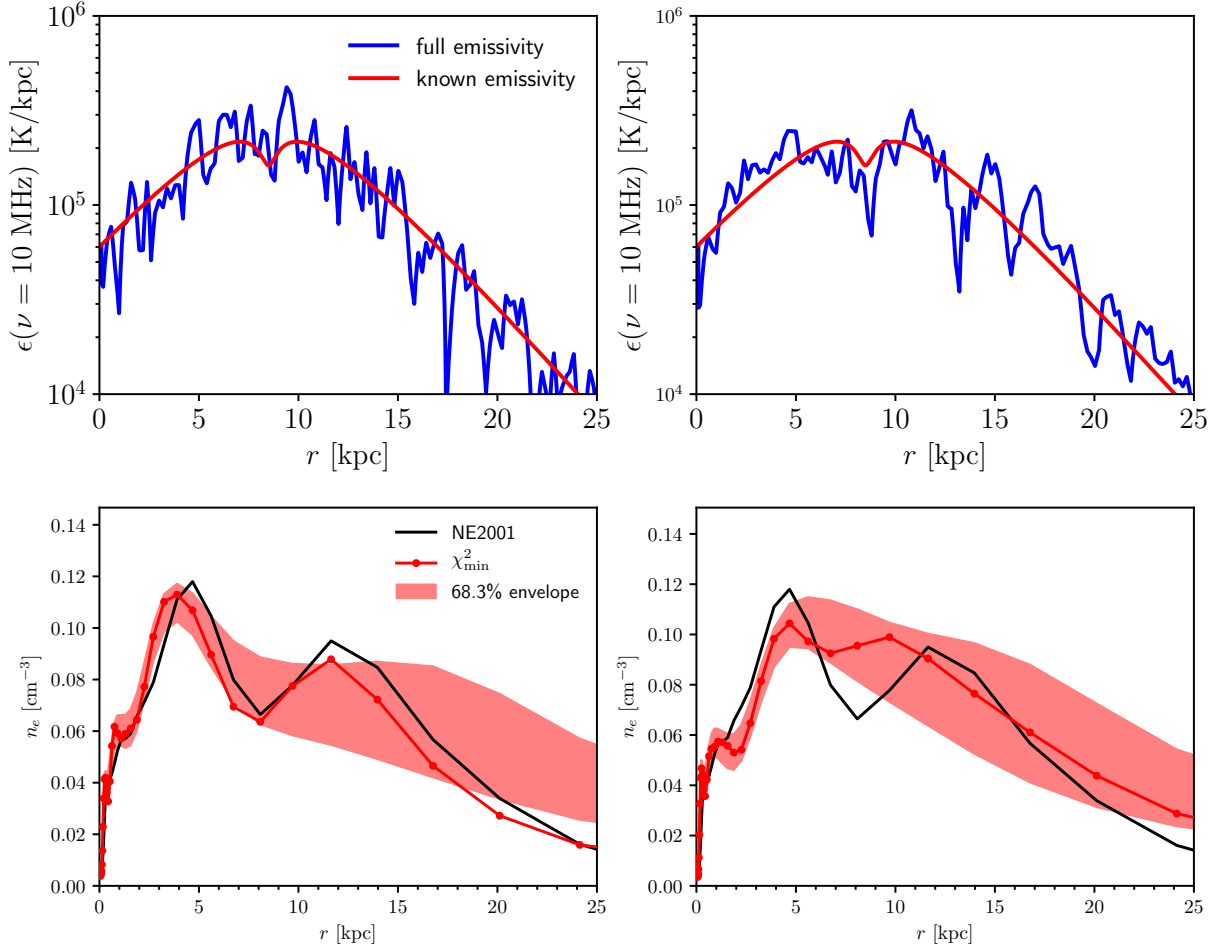


Figure 8. The emissivity with small-scale fluctuations and its known smooth component (top panels), and the reconstructed electron density profiles for the LoS with $l = 2.0^\circ$ on Galactic plane (bottom panels). For left panels we adopt $k_{\min} = 5.0 \text{ kpc}^{-1}$ and for right panels we adopt $k_{\min} = 0.5 \text{ kpc}^{-1}$. All density profiles, including the NE2001, have been smoothed by a Gaussian kernel with radius equal to one bin.

Capitaniao, L., Lallement, R., Vergely, J. L., Elyajouri, M., & Monreal-Ibero, A. 2017, *A&A*, 606, A65, doi: [10.1051/0004-6361/201730831](https://doi.org/10.1051/0004-6361/201730831)

Chen, X., Yan, J., Deng, L., et al. 2020, *Phil. Trans. Roy. Soc. Lond. A*, 379, 20190566, doi: [10.1098/rsta.2019.0566](https://doi.org/10.1098/rsta.2019.0566)

Chen, X., Burns, J., Koopmans, L., et al. 2019, arXiv e-prints, arXiv:1907.10853. <https://arxiv.org/abs/1907.10853>

Condon, J. J., & Ransom, S. M. 2016, *Essential Radio Astronomy*

Cong, Y., Yue, B., Xu, Y., et al. 2021, *ApJ*, 914, 128, doi: [10.3847/1538-4357/abf55c](https://doi.org/10.3847/1538-4357/abf55c)

Cordes, J. M., & Lazio, T. J. W. 2002, arXiv e-prints, astro. <https://arxiv.org/abs/astro-ph/0207156>

—, 2003, arXiv e-prints, astro.

<https://arxiv.org/abs/astro-ph/0301598>

Cordes, J. M., Weisberg, J. M., Frail, D. A., Spangler, S. R., & Ryan, M. 1991, *Nature*, 354, 121, doi: [10.1038/354121a0](https://doi.org/10.1038/354121a0)

Cox, D. P., & Reynolds, R. J. 1987, *ARA&A*, 25, 303, doi: [10.1146/annurev.aa.25.090187.001511](https://doi.org/10.1146/annurev.aa.25.090187.001511)

de Oliveira-Costa, A., Tegmark, M., Gaensler, B. M., et al. 2008, *MNRAS*, 388, 247, doi: [10.1111/j.1365-2966.2008.13376.x](https://doi.org/10.1111/j.1365-2966.2008.13376.x)

Dickinson, C., Davies, R. D., & Davis, R. J. 2003, *MNRAS*, 341, 369, doi: [10.1046/j.1365-8711.2003.06439.x](https://doi.org/10.1046/j.1365-8711.2003.06439.x)

Draine, B. T. 2011, *Physics of the Interstellar and Intergalactic Medium*

Ellis, G. R. A. 1982, *Australian Journal of Physics*, 35, 91, doi: [10.1071/PH820091](https://doi.org/10.1071/PH820091)

Ellis, G. R. A., & Hamilton, P. A. 1964, *Nature*, 204, 272, doi: [10.1038/204272a0](https://doi.org/10.1038/204272a0)

—, 1966a, *ApJ*, 143, 227, doi: [10.1086/148493](https://doi.org/10.1086/148493)

—, 1966b, *ApJ*, 146, 78, doi: [10.1086/148860](https://doi.org/10.1086/148860)

Ellis, G. R. A., Waterworth, M. D., & Bessell, M. 1962, *Nature*, 196, 1079, doi: [10.1038/1961079a0](https://doi.org/10.1038/1961079a0)

Englmaier, P., Pohl, M., & Bissantz, N. 2011, *Memorie della Societa Astronomica Italiana Supplementi*, 18, 199. <https://arxiv.org/abs/0812.3491>

Ferrière, K. M. 2001, *Reviews of Modern Physics*, 73, 1031, doi: [10.1103/RevModPhys.73.1031](https://doi.org/10.1103/RevModPhys.73.1031)

- Finkbeiner, D. P. 2003, *ApJS*, 146, 407, doi: [10.1086/374411](https://doi.org/10.1086/374411)
- Fleishman, G. D., & Tokarev, Y. V. 1995, *A&A*, 293, 565
- Foreman-Mackey, D., Hogg, D. W., Lang, D., & Goodman, J. 2013, *PASP*, 125, 306, doi: [10.1086/670067](https://doi.org/10.1086/670067)
- Frisch, P. C., Redfield, S., & Slavin, J. D. 2011, *ARA&A*, 49, 237, doi: [10.1146/annurev-astro-081710-102613](https://doi.org/10.1146/annurev-astro-081710-102613)
- Gaensler, B. M., Madsen, G. J., Chatterjee, S., & Mao, S. A. 2008, *PASA*, 25, 184, doi: [10.1071/AS08004](https://doi.org/10.1071/AS08004)
- Gaia Collaboration, Drimmel, R., Romero-Gomez, M., et al. 2022, arXiv e-prints, arXiv:2206.06207. <https://arxiv.org/abs/2206.06207>
- George, M., Orchiston, W., Slee, B., & Wielebinski, R. 2015a, *Journal of Astronomical History and Heritage*, 18, 14
- . 2015b, *Journal of Astronomical History and Heritage*, 18, 177
- . 2016, *Journal of Astronomical History and Heritage*, 19, 185
- George, M., Orchiston, W., Wielebinski, R., & Slee, B. 2015c, *Journal of Astronomical History and Heritage*, 18, 312
- Ghisellini, G. 2013, *Radiative Processes in High Energy Astrophysics*, Vol. 873, doi: [10.1007/978-3-319-00612-3](https://doi.org/10.1007/978-3-319-00612-3)
- Gómez, G. C., Benjamin, R. A., & Cox, D. P. 2001, *AJ*, 122, 908, doi: [10.1086/321180](https://doi.org/10.1086/321180)
- Greiner, M., Schnitzeler, D. H. F. M., & Enßlin, T. A. 2016, *A&A*, 590, A59, doi: [10.1051/0004-6361/201526717](https://doi.org/10.1051/0004-6361/201526717)
- Haffner, L. M., Reynolds, R. J., Tufte, S. L., et al. 2003, *ApJS*, 149, 405, doi: [10.1086/378850](https://doi.org/10.1086/378850)
- Haffner, L. M., Dettmar, R. J., Beckman, J. E., et al. 2009, *Reviews of Modern Physics*, 81, 969, doi: [10.1103/RevModPhys.81.969](https://doi.org/10.1103/RevModPhys.81.969)
- Hartz, T. R. 1964, *Nature*, 203, 173, doi: [10.1038/203173a0](https://doi.org/10.1038/203173a0)
- Haslam, C. G. T., Salter, C. J., Stoffel, H., & Wilson, W. E. 1982, *A&AS*, 47, 1
- Hindson, L., Johnston-Hollitt, M., Hurley-Walker, N., et al. 2016, *PASA*, 33, e020, doi: [10.1017/pasa.2016.19](https://doi.org/10.1017/pasa.2016.19)
- Hou, L. G., & Han, J. L. 2014, *A&A*, 569, A125, doi: [10.1051/0004-6361/201424039](https://doi.org/10.1051/0004-6361/201424039)
- Hoyle, F., & Ellis, G. R. A. 1963, *Australian Journal of Physics*, 16, 1, doi: [10.1071/PH630001](https://doi.org/10.1071/PH630001)
- Iacobelli, M., Haverkorn, M., Orrú, E., et al. 2013, *A&A*, 558, A72, doi: [10.1051/0004-6361/201322013](https://doi.org/10.1051/0004-6361/201322013)
- Jester, S., & Falcke, H. 2009, *NewAR*, 53, 1, doi: [10.1016/j.newar.2009.02.001](https://doi.org/10.1016/j.newar.2009.02.001)
- Jones, D. I., Igoshev, A. P., & Haverkorn, M. 2016, *MNRAS*, 460, 3298, doi: [10.1093/mnras/stw1192](https://doi.org/10.1093/mnras/stw1192)
- Kassim, N. E. 1989, *ApJ*, 347, 915, doi: [10.1086/168183](https://doi.org/10.1086/168183)
- Kulkarni, S. R., & Heiles, C. 1988, in *Galactic and Extragalactic Radio Astronomy*, ed. K. I. Kellermann & G. L. Verschuur, 95–153
- Lallement, R., Vergely, J. L., Valette, B., et al. 2014, *A&A*, 561, A91, doi: [10.1051/0004-6361/201322032](https://doi.org/10.1051/0004-6361/201322032)
- Manning, R., & Dulk, G. A. 2001, *A&A*, 372, 663, doi: [10.1051/0004-6361:20010516](https://doi.org/10.1051/0004-6361:20010516)
- Miller, M. J., & Bregman, J. N. 2013, *ApJ*, 770, 118, doi: [10.1088/0004-637X/770/2/118](https://doi.org/10.1088/0004-637X/770/2/118)
- Nakanishi, H., & Sofue, Y. 2016, *PASJ*, 68, 5, doi: [10.1093/pasj/psv108](https://doi.org/10.1093/pasj/psv108)
- Nord, M. E., Henning, P. A., Rand, R. J., Lazio, T. J. W., & Kassim, N. E. 2006, *AJ*, 132, 242, doi: [10.1086/504407](https://doi.org/10.1086/504407)
- Nordgren, T. E., Cordes, J. M., & Terzian, Y. 1992, *AJ*, 104, 1465, doi: [10.1086/116331](https://doi.org/10.1086/116331)
- Novaco, J. C., & Brown, L. W. 1978, *ApJ*, 221, 114, doi: [10.1086/156009](https://doi.org/10.1086/156009)
- Ocker, S. K., Cordes, J. M., & Chatterjee, S. 2020, *ApJ*, 897, 124, doi: [10.3847/1538-4357/ab98f9](https://doi.org/10.3847/1538-4357/ab98f9)
- . 2021, *ApJ*, 911, 102, doi: [10.3847/1538-4357/abeb6e](https://doi.org/10.3847/1538-4357/abeb6e)
- Orchiston, W., George, M., Slee, B., & Wielebinski, R. 2015a, *Journal of Astronomical History and Heritage*, 18, 3
- Orchiston, W., Slee, B., George, M., & Wielebinski, R. 2015b, *Journal of Astronomical History and Heritage*, 18, 285
- Orlando, E., & Strong, A. 2013a, *MNRAS*, 436, 2127, doi: [10.1093/mnras/stt1718](https://doi.org/10.1093/mnras/stt1718)
- Orlando, E., & Strong, A. W. 2013b, in *International Cosmic Ray Conference*, Vol. 33, *International Cosmic Ray Conference*, 841. <https://arxiv.org/abs/1307.2264>
- Peron, G., Aharonian, F., Casanova, S., Yang, R., & Zanin, R. 2021, *ApJL*, 907, L11, doi: [10.3847/2041-8213/abcaa9](https://doi.org/10.3847/2041-8213/abcaa9)
- Peterson, J. D., & Webber, W. R. 2002, *ApJ*, 575, 217, doi: [10.1086/341258](https://doi.org/10.1086/341258)
- Polderman, I. M., Haverkorn, M., Jaffe, T. R., & Alves, M. I. R. 2019, *A&A*, 621, A127, doi: [10.1051/0004-6361/201834405](https://doi.org/10.1051/0004-6361/201834405)
- Porter, T. A., Johannesson, G., & Moskalenko, I. V. 2021, arXiv e-prints, arXiv:2112.12745. <https://arxiv.org/abs/2112.12745>
- Reber, G. 1994, *JRASC*, 88, 297
- Reber, G., & Ellis, G. R. 1956, *J. Geophys. Res.*, 61, 1, doi: [10.1029/JZ061i001p00001](https://doi.org/10.1029/JZ061i001p00001)
- Remazeilles, M., Dickinson, C., Banday, A. J., Bigot-Sazy, M. A., & Ghosh, T. 2015, *MNRAS*, 451, 4311, doi: [10.1093/mnras/stv1274](https://doi.org/10.1093/mnras/stv1274)
- Reynolds, R. J. 1977, *ApJ*, 216, 433, doi: [10.1086/155484](https://doi.org/10.1086/155484)
- . 1990, in *Low Frequency Astrophysics from Space*, ed. N. E. Kassim & K. W. Weiler, Vol. 362, 121, doi: [10.1007/3-540-52891-1](https://doi.org/10.1007/3-540-52891-1)
- . 1991a, *ApJL*, 372, L17, doi: [10.1086/186013](https://doi.org/10.1086/186013)
- Reynolds, R. J. 1991b, in *The Interstellar Disk-Halo Connection in Galaxies*, ed. H. Bloemen, Vol. 144, 67
- Reynolds, R. J., & Haffner, L. M. 2000, arXiv e-prints, astro. <https://arxiv.org/abs/astro-ph/0010618>
- Rezaei Kh., S., Bailer-Jones, C. A. L., Hogg, D. W., & Schultheis, M. 2018, *A&A*, 618, A168, doi: [10.1051/0004-6361/201833284](https://doi.org/10.1051/0004-6361/201833284)
- Sarkar, K. C. 2019, *MNRAS*, 482, 4813, doi: [10.1093/mnras/sty2944](https://doi.org/10.1093/mnras/sty2944)

- Schnitzeler, D. H. F. M. 2012, MNRAS, 427, 664, doi: [10.1111/j.1365-2966.2012.21869.x](https://doi.org/10.1111/j.1365-2966.2012.21869.x)
- Seiffert, M., Fixsen, D. J., Kogut, A., et al. 2011, ApJ, 734, 6, doi: [10.1088/0004-637X/734/1/6](https://doi.org/10.1088/0004-637X/734/1/6)
- Shi, Y., Deng, F., Xu, Y., et al. 2022a, ApJ, 929, 32, doi: [10.3847/1538-4357/ac5965](https://doi.org/10.3847/1538-4357/ac5965)
- Shi, Y., Xu, Y., Deng, L., et al. 2022b, MNRAS, 510, 3046, doi: [10.1093/mnras/stab3623](https://doi.org/10.1093/mnras/stab3623)
- Singal, J., Haider, J., Ajello, M., et al. 2018, PASP, 130, 036001, doi: [10.1088/1538-3873/aaa6b0](https://doi.org/10.1088/1538-3873/aaa6b0)
- Smith, F. G. 1965, MNRAS, 131, 145, doi: [10.1093/mnras/131.1.145](https://doi.org/10.1093/mnras/131.1.145)
- Snowden, S. L., Egger, R., Finkbeiner, D. P., Freyberg, M. J., & Plucinsky, P. P. 1998, ApJ, 493, 715, doi: [10.1086/305135](https://doi.org/10.1086/305135)
- Su, H., Hurley-Walker, N., Jackson, C. A., et al. 2017, MNRAS, 465, 3163, doi: [10.1093/mnras/stw2959](https://doi.org/10.1093/mnras/stw2959)
- Su, H., Macquart, J. P., Hurley-Walker, N., et al. 2018, MNRAS, 479, 4041, doi: [10.1093/mnras/sty1732](https://doi.org/10.1093/mnras/sty1732)
- Sun, X. H., Reich, W., Waelkens, A., & Enßlin, T. A. 2008, A&A, 477, 573, doi: [10.1051/0004-6361:20078671](https://doi.org/10.1051/0004-6361:20078671)
- Taylor, J. H., & Cordes, J. M. 1993, ApJ, 411, 674, doi: [10.1086/172870](https://doi.org/10.1086/172870)
- Toscano, M., Britton, M. C., Manchester, R. N., et al. 1999, ApJL, 523, L171, doi: [10.1086/312276](https://doi.org/10.1086/312276)
- Williamson, I. P. 1972, MNRAS, 157, 55, doi: [10.1093/mnras/157.1.55](https://doi.org/10.1093/mnras/157.1.55)
- Woermann, B. 1998, PhD thesis, Rhodes University, South Africa
- Wolleben, M. 2007, ApJ, 664, 349, doi: [10.1086/518711](https://doi.org/10.1086/518711)
- Yao, J. M., Manchester, R. N., & Wang, N. 2017, ApJ, 835, 29, doi: [10.3847/1538-4357/835/1/29](https://doi.org/10.3847/1538-4357/835/1/29)
- Zucker, C., Goodman, A. A., Alves, J., et al. 2022, Nature, 601, 334, doi: [10.1038/s41586-021-04286-5](https://doi.org/10.1038/s41586-021-04286-5)